Research Square

Preprints are preliminary reports that have not undergone peer review.
They should not be considered conclusive, used to inform clinical practice,
or referenced by the media as validated information.

Exact Potential of Spherical Resistor Networks and Potential-Guided Path Planning

Jiahan liao
Linyi University
Xiaoyu Jiang
jxy19890422@sina.com

Linyi University
Yanpeng Zheng
Linyi University
Zhaolin Jiang
Shandong Vocational and Technical University of International Studies

Research Article

Keywords: Spherical resistor network, Exact nodal potential, Potential-guided path planning, Dynamic obstacle avoidance

Posted Date: October 1st, 2026

DOI: https://doi.org/10.21203/rs.3.rs-11079821/v1

License: This work is licensed under a Creative Commons Attribution 4.0 International License.
Read Full License

Additional Declarations: No competing interests reported.

Exact Potential of Spherical Resistor Networks and Potential-Guided Path Planning

Abstract

Resistor networks provide an important physical model for characterizing transport behavior and connectivity in complex systems. Their nodal potentials link discrete network structures with global steady-state responses, thereby providing a basis for transforming physical information into computation and decision making. Motivated by this property, this work investigates a class of spherical superstructured quadrilateral resistor network (SSQRN). By exploiting the spectral structure of the network Laplacian, the nodal potentials are derived and a complete exact physical potential field is obtained. It is further shown that no non-sink node can be a strict local minimum of the potential field, and that every equipotential connected component not containing the sink possesses a boundary exit leading to a region of strictly lower potential. These properties establish a theoretical basis for potential-descent-based path guidance. On this basis, a resistor network potential-guided planning method (RNPG) is proposed to transform the global connectivity information encoded in the physical potential field into local navigation decisions. Experimental results show that RNPG achieves high planning efficiency while maintaining stable planning success rates and path quality. On a 100×100 grid, its median search time is only 0.001168 s. In addition, the proposed method is successfully extended to environments with dynamic obstacles. By integrating the exact potential field of SSQRN with path planning, this work provides a new framework for physics-driven, efficient, and interpretable navigation.

Keywords: Spherical resistor network, Exact nodal potential, Potential-guided path planning, Dynamic obstacle avoidance

1 Introduction

Resistor networks, serving as a foundational and powerful modelling and analysis tool, play an indispensable role in modern science and engineering. Owing to their proven stability, repeatability, and precision, the analytical methods derived from resistor networks have permeated a wide spectrum of fields, from fundamental science to engineering applications. At the fundamental theoretical level, the study of resistor networks hold significant value across multiple domains. It supports research on nonlinear topological circuits and optoelectronic applications[1] and is used to analyse

defect effects in topological insulators[2]. Most notably, the study of graphene networks, a typical two-dimensional resistor system, is foundational, with A. K. Geim?s work earning a Nobel Prize[3, 4], further highlighting the central role of resistor networks as a fundamental physical model. In engineering applications, resistor network modeling can be used for performance prediction, optimization, and state diagnosis at the materials and device level, covering thin-film defect analysis in organic electronics[5], equivalent-circuit characterization of PCB gratings[6], and optimization of microstrip reflector-antenna designs[7].It is also applied to evaluating the performance of solid-oxide fuel cells (SOFCs)[8] and to damage localization by simulating resistance changes in Carbon Fiber Reinforced Polymer (CFRP)[9]. At the system-application level, resistor network?based electrical analysis can mitigate position distortion in γ-ray imaging localization, demonstrating its value in complex systems[10]. Among these studies, nodal potential is a particularly important physical quantity because it not only reflects the influence of local branch parameters, but also comprehensively characterizes the global steady-state response induced by the entire network topology.

Since Kirchhoff established the fundamental laws of electrical circuits[11], how to obtain the exact response of complex resistor networks have remained an important problem in electrical network theory. Wu established an exact solution framework for finite regular resistor networks based on the Laplacian operator[12]; subsequently, Izmailian and Kenna further generalized the Laplacian method, enabling it to deal with network structures having more complex boundary conditions[13]. These studies demonstrate that the structure and spectral representation of the network Laplacian provide an effective approach for obtaining the exact steady-state responses of complex resistor networks.

Spherical structures possess characteristics such as isotropy, closed surfaces, and geometric symmetry, and have been widely used in underwater acoustics, spherical sensing, and aerospace applications[14–16]. Therefore, extending resistor network topologies to spherical surfaces not only has a clear geometric and physical background, but also provides a representative discrete model for studying steady-state responses in complex curved-surface structures.

The spherical resistor network considered in this work simultaneously contains circumferential periodic connections and special polar boundaries. Such topological characteristics distinguish it from conventional planar regular grids and also make the exact solution of nodal potentials more complex. In particular, considering only the spectral response of the internal nodes cannot completely describe the physical potential of the entire network, and the additional contribution induced by the polar boundaries must also be taken into account. Therefore, obtaining an exact nodal potential that incorporates all boundary effects is fundamental to further investigating the physical properties and applications of this class of spherical resistor networks.

On the other hand, with the development of robotic inspection, surface monitoring, and autonomous motion tasks, how to achieve safe and efficient path planning in spherical and other curved-surface environments has become a problem of increasing practical importance. Compared with conventional planar environments, motion on curved surfaces is affected not only by obstacle distributions, but also by factors

such as surface topology, discrete representation, and computational efficiency. Therefore, developing efficient navigation methods for spherical environments has important theoretical significance and engineering value.

From the perspective of topology, spherical resistor networks can also be regarded as a class of superstructured quadrilateral meshes with special boundary connections. In recent years, superstructured quadrilateral meshes have attracted increasing attention because they combine regular local connectivity with complex global topological characteristics[17–19]. Meanwhile, studies on higher-order network dynamics have shown that complex network topologies and their collective responses can provide new theoretical foundations for physics-inspired computational mechanisms[20, 21].

Therefore, investigating the exact physical response and subsequent navigation mechanism of the spherical superstructured quadrilateral resistor network (SSQRN) not only concerns the analytical problem of the spherical resistor network itself, but also contributes to a deeper understanding of the relationships among complex network topology, global physical responses, and computational decision making.

Existing discrete path-planning methods mainly rely on graph-search strategies. Dijkstra's[22] algorithm lacks goal-directed heuristic information and therefore usually expands a relatively large number of nodes in large-scale search spaces; A*[23] reduces the search region through a heuristic function, but its computational cost still increases with map size and obstacle complexity; Jump Point Search (JPS)[24] improves the search efficiency of A* by exploiting symmetry in regular grids, but complex obstacle distributions can reduce the effectiveness of its jumping and pruning mechanisms. In general, these methods still need to explicitly explore the search space during the planning process, and their computational costs are closely related to the scale and complexity of the environment. For surface motion tasks that need frequent planning or quick reactions, figuring out how to lighten the search load, boost planning efficiency, and respond quickly while still keeping a good planning success rate and decent path quality is still something worth looking into.

The potential field of a resistor network provides another possible approach to this problem[25–27]. When a spherical surface is discretized into a resistor network with a prescribed connectivity, the nodal potential generated by source–sink excitation is not an artificially assigned local cost, but rather a global steady-state response jointly determined by the entire network topology, branch parameters, and boundary conditions[28–33]. Therefore, the nodal potential naturally contains global information encoded by the network connectivity. This property enables the same physical potential field to adapt to different scenarios on the same map, providing a new possibility for constructing efficient and physically interpretable path-planning methods.

However, several key issues remain to be addressed for the SSQRN considered in this work. First, a complete exact potential incorporating both the internal spectral response and the contribution of the polar boundaries needs to be established. Second, it is necessary to further clarify whether this physical potential field possesses a reliable navigation structure, particularly whether an exit toward a region of lower potential still exists when multiple nodes form an equipotential plateau. Finally, it is necessary to investigate how to effectively separate the fixed physical potential field from varying

obstacle constraints, so that the same potential field can be reused under different static and even dynamic obstacle environments.

Based on the above issues, this work establishes a unified framework that integrates exact potential analysis of the SSQRN with RNPG path planning.

The main contributions of this work are summarized as follows:

1. For the SSQRN, a complete exact nodal-potential expression incorporating the contribution of the special polar boundaries is established. Numerical validation shows that the resulting complete potential satisfies the network equations with errors close to machine precision.
2. The navigation properties of the exact physical potential field are further investigated. It is proved that no non-sink node can be a strict local minimum, which follows from the discrete harmonic property. It is further proved that every equipotential connected component not containing the sink possesses a boundary exit leading to a region of strictly lower potential, thereby providing a more complete theoretical basis for potential-descent navigation.
3. A resistor network potential-guided planning method, denoted as RNPG, is proposed. The method transforms the global network information contained in the exact physical potential field into local motion decisions, greatly improving the computational efficiency in complex obstacle environments.
4. Experiments have verified that RNPG achieves high planning efficiency and real-time responsiveness in the tested static environment, while maintaining a stable planning success rate and path quality. In addition, the method is successfully extended to dynamic-obstacle environments.

The remainder of this paper is organized as follows. Section 2 introduces the SSQRN model and derives the complete exact potential. Section 3 analyzes the navigation properties of the physical potential field. Section 4 presents the RNPG path-planning method. Section 5 reports the static and dynamic path-planning experiments. Finally, Section 6 concludes the paper and discusses future research directions. The research methodology of this paper is illustrated in Figure 1.

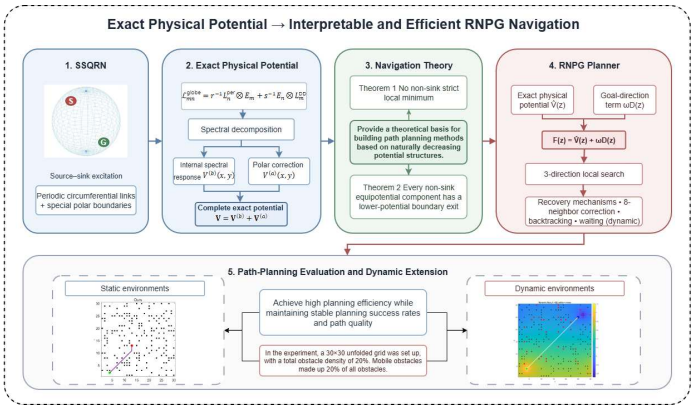


Fig. 1: Overall research framework and workflow.

2 SSQRN and exact potential field

This section introduces SSQRN and derives the exact expression for the node potential correction induced by non-reference extreme nodes under source-sink excitation.

2.1 SSQRN network configuration and source–sink excitation

We first introduce the $m \times n$ spherical resistor network proposed by N. Sh. Izmailian and R. Kenna [13], as illustrated in Figure 2. The network consists of mn internal nodes and two additional polar nodes, denoted by P_{N} and P_{S}.

Fig. 2: Schematic of the $m \times n$ SSQRN with mn internal nodes and two polar nodes.

An internal node located at the intersection of the x-th circumferential position and the y-th meridional layer is denoted by $A(x, y)$, where $x = 1, 2, \ldots, n, y = 1, 2, \ldots, m$. The circumferential direction satisfies the periodic identification $A(n + 1, y) \equiv A(1, y), A(0, y) \equiv A(n, y)$.

For subsequent matrix representation, the two-dimensional node $A(x, y)$ is mapped to the one-dimensional index

$$k = m(x - 1) + y, \qquad k = 1, 2, \ldots, mn. \tag{1}$$

Adjacent nodes in the circumferential direction are connected by resistors of resistance r, whereas adjacent nodes in the meridional direction are connected by resistors of resistance s. The nodes $A(x, 1)$ are connected to the north pole P_{N}, while the nodes $A(x, m)$ are connected to the south pole P_{S}, with the corresponding polar branches also having resistance s.

The source–sink current excitation is imposed on two arbitrary internal nodes. Let $A_s = A(x_s, y_s), A_g = A(x_g, y_g)$ denote the source and sink nodes, respectively. A current of magnitude $I_{\mathrm{amp}} > 0$ is injected at A_s and extracted at A_g. Thus, the external current at an internal node $A(x, y)$ is

$$I(x, y) = I_{\mathrm{amp}} \left[\delta_{x,x_s}\delta_{y,y_s} - \delta_{x,x_g}\delta_{y,y_g}\right], \tag{2}$$

where $\delta_{\cdot,\cdot}$ denotes the Kronecker delta. Consequently,

$$\sum_{x=1}^{n}\sum_{y=1}^{m} I(x, y) = 0.$$

In the path-planning interpretation developed later, A_s and A_g will correspond to the start and goal nodes, respectively.

According to Kirchhoff's current law, the nodal equation of the complete resistor network can be written as

$$\sum_j c_{ij}(V_i - V_j) = I_i, \tag{3}$$

where V_i and I_i denote the potential and externally injected current at node i, respectively, and $c_{ij} = c_{ji}$ is the branch conductance between nodes i and j.

2.2 Exact potential field

2.2.1 Reduced Laplacian formulation

Because the complete network is connected and satisfies current conservation, its global Laplacian matrix has a one-dimensional null space. To remove the resulting gauge freedom, the south pole P_{S} is selected as the reference node and its potential is set to zero, $V_{\mathrm{S}} = 0$. The potential of the north pole is denoted by V_0.

After separating the two polar nodes, define the internal nodal-potential vector $\mathbf{V} = (V_1, V_2, \ldots, V_{mn})^{\mathrm{T}}$ and the internal current-injection vector $\mathbf{I} = (I_1, I_2, \ldots, I_{mn})^{\mathrm{T}}$.

The reduced Laplacian associated with the mn internal nodes is

$$\mathcal{L}_{mn}^{\mathrm{globe}} = r^{-1} L_n^{\mathrm{per}} \otimes E_m + s^{-1} E_n \otimes L_m^{\mathrm{DD}}, \tag{4}$$

where E_n and E_m denote the identity matrices of orders n and m, respectively.

Here,

$$L_n^{\mathrm{per}} = \begin{pmatrix} 2 & -1 & 0 & \cdots & 0 & -1 \\ -1 & 2 & -1 & \ddots & 0 & 0 \\ 0 & \ddots & \ddots & \ddots & \ddots & \vdots \\ \vdots & \ddots & \ddots & \ddots & \ddots & 0 \\ 0 & 0 & \ddots & -1 & 2 & -1 \\ -1 & 0 & \cdots & 0 & -1 & 2 \end{pmatrix}_{n \times n} \tag{5}$$

is the one-dimensional discrete Laplacian with periodic boundary conditions, whereas

$$L_m^{\mathrm{DD}} = \begin{pmatrix} 2 & -1 & 0 & \cdots & 0 & 0 \\ -1 & 2 & -1 & \ddots & 0 & 0 \\ 0 & \ddots & \ddots & \ddots & \ddots & \vdots \\ \vdots & \ddots & \ddots & \ddots & \ddots & 0 \\ 0 & 0 & \ddots & -1 & 2 & -1 \\ 0 & 0 & \cdots & 0 & -1 & 2 \end{pmatrix}_{m \times m} \tag{6}$$

is the one-dimensional discrete Laplacian with Dirichlet–Dirichlet boundary conditions.

Following the generalized Laplacian formulation of Izmailian and Kenna [13], the Kronecker-sum matrix in Eq. (4) is diagonalized by the tensor product of the Fourier basis in the periodic direction and the discrete sine basis in the meridional direction. With $\theta_p = 2\pi p/n$ $(p = 0, \ldots, n-1)$ and $\phi_q = q\pi/(m+1)$ $(q = 1, \ldots, m)$, the normalized eigenmodes and eigenvalues are

$$\psi_{pq}(x,y) = \sqrt{\frac{2}{n(m+1)}} e^{\mathrm{i}(x-1)\theta_p} \sin(y\phi_q), \quad \lambda_{pq} = \frac{2}{r}(1-\cos\theta_p) + \frac{2}{s}(1-\cos\phi_q). \tag{7}$$

Since $\lambda_{pq} > 0$ for all (p, q), the reduced Laplacian is invertible, and the standard spectral expansion of its inverse can be directly used to obtain the exact nodal potential.

Since the north-pole potential V_0 is generally nonzero, the complete reduced equation for the internal nodes should be written as

$$\mathcal{L}_{mn}^{\mathrm{globe}} \mathbf{V} = \mathbf{I} + V_0 \mathbf{c}_{\mathrm{N}}, \tag{8}$$

where $\mathbf{c}_{\mathrm{N}}$ represents the coupling between the internal nodes and the north pole. For the indexing rule in Eq. (1), its components satisfy

$$(\mathbf{c}_{\mathrm{N}})_{m(x-1)+y} = \begin{cases} s^{-1}, & y = 1, \\ 0, & y = 2, \ldots, m, \end{cases} \qquad x = 1, \ldots, n. \tag{9}$$

Eq. (8) makes explicit that the internal potential consists of two contributions. Accordingly, we write

$$\mathbf{V} = \mathbf{V}^{(b)} + \mathbf{V}^{(a)}, \tag{10}$$

where $\mathbf{V}^{(b)} = \left(\mathcal{L}_{mn}^{\mathrm{globe}}\right)^{-1} \mathbf{I}, \mathbf{V}^{(a)} = V_0 \left(\mathcal{L}_{mn}^{\mathrm{globe}}\right)^{-1} \mathbf{c}_{\mathrm{N}}$.

The term $\mathbf{V}^{(b)}$ describes the direct response to the internal source–sink excitation, whereas $\mathbf{V}^{(a)}$ accounts for the boundary correction induced by the non-reference polar potential.

2.2.2 Exact nodal potential with polar correction

We now derive the exact potential generated by the source–sink excitation in Eq. (2). For the source node $A_s = A(x_s, y_s)$ and the sink node $A_g = A(x_g, y_g)$, the current-response component can be expressed through the spectral representation as

$$V^{(b)}(x,y) = I_{\mathrm{amp}} \sum_{p=0}^{n-1} \sum_{q=1}^{m} \frac{\psi_{pq}(x,y)\left[\psi_{pq}^*(x_s,y_s) - \psi_{pq}^*(x_g,y_g)\right]}{\lambda_{pq}}. \tag{11}$$

Using Eq. (7), the above expression can be written in an explicitly real form:

$$V^{(b)}(x,y) = \frac{2I_{\text{amp}}}{n(m+1)} \sum_{p=0}^{n-1} \sum_{q=1}^{m} \frac{\sin(y\phi_q)}{\lambda_{pq}} \times \Big[\sin(y_s\phi_q)\cos\big((x-x_s)\theta_p\big) - \sin(y_g\phi_q)\cos\big((x-x_g)\theta_p\big) \Big]. \tag{12}$$

Eq. (12) describes the exact response produced by the internal source–sink pair under homogeneous polar boundary conditions. However, the actual north-pole potential is generally nonzero and therefore induces an additional boundary contribution.

Because the polar excitation is uniform in the circumferential direction, only the zero circumferential mode contributes to $\mathbf{V}^{(a)}$. The resulting meridional potential varies linearly between the north pole V_0 and the reference south pole 0, yielding

$$V^{(a)}(x,y) = V_0 \frac{m+1-y}{m+1}. \tag{13}$$

For an internal source–sink pair, summing the Kirchhoff equations over each meridional layer and applying the zero-external-current condition at the polar nodes gives

$$V_0 = \frac{I_{\text{amp}} s}{n}(y_g - y_s). \tag{14}$$

Combining Eqs. (12), (13), and (14), the complete potential at an arbitrary internal node $A(x,y)$ is therefore

$$V(x,y) = \frac{2I_{\text{amp}}}{n(m+1)} \sum_{p=0}^{n-1} \sum_{q=1}^{m} \frac{\sin(y\phi_q)}{\lambda_{pq}} \times \Big[\sin(y_s\phi_q)\cos((x-x_s)\theta_p) - \sin(y_g\phi_q)\cos((x-x_g)\theta_p) \Big] + \frac{I_{\text{amp}} s (y_g - y_s)(m+1-y)}{n(m+1)}. \tag{15}$$

where $\theta_p = \frac{2\pi p}{n}, \phi_q = \frac{q\pi}{m+1}$, and λ_{pq} is given by Eq. (7).

Eq. (15) provides the exact steady-state potential at every internal node of the spherical resistor network for arbitrary internal source and sink locations. This potential field is jointly determined by the global network connectivity, branch resistances, spherical boundary conditions, and source–sink excitation.

2.3 Validation of the exact potential field

In this section, the analytical potential expression derived in Eq. (15) is numerically validated. Four grid sizes, $10\times10, 20\times20, 30\times30, 50\times50$, are considered. For each size, three resistance ratios $r/s = 0.1, 1, 10$ and three different source–sink pairs are tested.

Let $\mathbf{V}_{\text{exact}}$ denote the potential obtained from the Eq. (15), and let $\mathbf{V}_{\text{direct}}$ denote the numerical solution obtained by directly solving the reduced Laplacian system. The relative error is defined as $E_{\text{rel}} = \frac{\|\mathbf{V}_{\text{exact}} - \mathbf{V}_{\text{direct}}\|_2}{\|\mathbf{V}_{\text{direct}}\|_2}$, and the maximum absolute error is $E_{\max} = \max_k |V_{k,\text{exact}} - V_{k,\text{direct}}|$. Table 1 reports the worst error observed at each grid size.

Table 1: Validation of the exact potential expression.

Grid	max E_{rel}	max $E_{\max}$	$E_{\text{rel}}^{\text{nc}}$	R_{eq}
10×10	1.12×10^{-14}	5.72×10^{-15}	0.161–0.949	1.03×10^{-14}
20×20	5.19×10^{-14}	2.43×10^{-14}	0.170–0.951	2.23×10^{-14}
30×30	1.10×10^{-13}	5.52×10^{-14}	0.175–0.938	5.07×10^{-14}
50×50	5.84×10^{-13}	2.79×10^{-13}	0.178–0.935	1.19×10^{-13}

Here, $E_{\text{rel}}^{\text{nc}}$ denotes the relative error without correction, and R_{eq} denotes the maximum equation residual.

The complete analytical expression remains in close agreement with the direct numerical solution over all 36 test cases. Even for the largest 50×50 grid, the maximum relative error is only 5.84×10^{-13} and the maximum absolute error is 2.79×10^{-13}. The residual of the reduced Laplacian equation is also of order 10^{-13} or smaller.

To further examine the role of the polar correction, the internal source–sink response $V^{(b)}$ is also compared with the direct solution without adding the correction term. As illustrated in Figure 3.

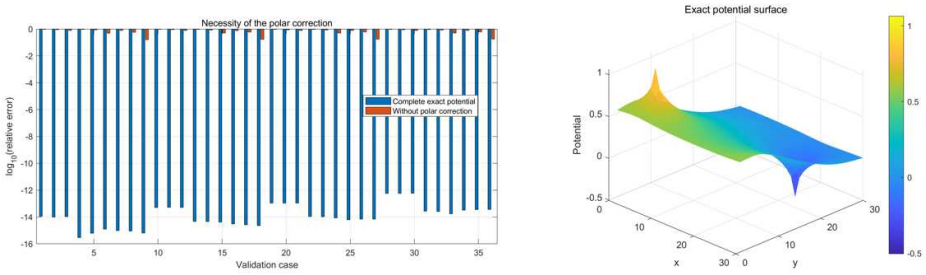


Fig. 3: Validation and visualization of the exact spherical-network potential: (a) exact potential surface; (b) necessity of the polar correction.

It can be seen from the figure, when the correction term is omitted, the relative error increases significantly, ranging from approximately 0.16 to 0.95, which is several orders of magnitude larger than that achieved by the complete expression. Therefore, the correction term is not a numerical refinement but an essential component required to recover the complete potential field of the spherical network.

3 Navigation properties of the exact potential field

For navigation, the current source A_s and the current sink A_g are interpreted as the start and goal nodes, respectively. We first establish the discrete harmonic property of the exact potential and then show that no non-sink node can be a strict local minimum. Furthermore, possible equipotential regions are considered, from which the existence of a non-increasing potential path toward the sink is established. These properties provide the theoretical foundation for the potential-guided path planner developed in the next section.

3.1 Discrete harmonic property of the potential field

Let $\overline{\Omega}$ denote the complete node set of the SSQRN, including the mn internal nodes and the two polar nodes. For a node $k \in \overline{\Omega}$, define its physical-neighbor set as

$$\mathcal{N}(k) = \{j \in \overline{\Omega} : c_{kj} > 0\}, \tag{16}$$

where $c_{kj} = c_{jk} > 0$ denotes the conductance of the branch connecting nodes k and j.

According to Kirchhoff's current law, the exact potential derived in Section 2 satisfies

$$\sum_{j \in \mathcal{N}(k)} c_{kj} \left(V_k - V_j\right) = I_{\text{amp}} \left(\delta_{k,s} - \delta_{k,g}\right), \tag{17}$$

where s and g denote the source and sink nodes, respectively.

For convenience, define the weighted degree of node k as $d_k = \sum_{j \in \mathcal{N}(k)} c_{kj}$, and introduce the normalized conductance $\omega_{kj} = \frac{c_{kj}}{d_k}, j \in \mathcal{N}(k)$. Since all branch resistances are positive, $\omega_{kj} > 0, \sum_{j \in \mathcal{N}(k)} \omega_{kj} = 1$.

For every node k that is neither the source nor the sink, Eq. (17) reduces to

$$\sum_{j \in \mathcal{N}(k)} c_{kj}(V_k - V_j) = 0. \tag{18}$$

Therefore,

$$V_k = \sum_{j \in \mathcal{N}(k)} \omega_{kj} V_j \qquad k \neq s, g. \tag{19}$$

Eq. (19) shows that the potential at every ordinary node is a strictly positive weighted average of the potentials at its physical neighboring nodes. Thus, the exact potential field is discrete harmonic at all nodes except the source and sink.

At the source node, Eq. (17) gives

$$\sum_{j \in \mathcal{N}(s)} \omega_{sj} V_j = V_s - \frac{I_{\text{amp}}}{d_s} < V_s, \tag{20}$$

whereas at the sink node,

$$\sum_{j\in\mathcal{N}(g)} \omega_{gj} V_j = V_g + \frac{I_{\mathrm{amp}}}{d_g} > V_g. \tag{21}$$

These relations provide a physical interpretation of the potential field: the source behaves as a high-potential excitation, the sink behaves as a low-potential excitation, and the ordinary nodes interpolate the global source–sink response through the resistor network connectivity.

3.2 Absence of strict local minima at non-sink nodes

For the resistor network potential considered here, the local-minimum problem can be analyzed directly from the Kirchhoff equations.

Theorem 1 *Consider a connected spherical resistor network in which every branch resistance is positive. Let V_k denote the exact potential generated by a current $I_{\mathrm{amp}} > 0$ injected at the source node s and extracted at the sink node g. Then no node $k \neq g$ is a strict local minimum of the potential field.*

Proof We first consider an ordinary node $k \neq s, g$. Suppose, by contradiction, that k is a strict local minimum. Then

$$V_k < V_j, \qquad \forall j \in \mathcal{N}(k). \tag{22}$$

Multiplying each inequality by the corresponding positive weight ω_{kj} and summing over all neighboring nodes yields

$$V_k < \sum_{j\in\mathcal{N}(k)} \omega_{kj} V_j. \tag{23}$$

However, according to the discrete harmonic relation (19),

$$\sum_{j\in\mathcal{N}(k)} \omega_{kj} V_j = V_k,$$

which leads to the contradiction $V_k < V_k$. Hence, an ordinary node cannot be a strict local minimum.

It remains to examine the source node. According to Eq. (20),

$$\sum_{j\in\mathcal{N}(s)} \omega_{sj} V_j < V_s. \tag{24}$$

If the source node were a local minimum, one would have $V_j \geq V_s$ for every $j \in \mathcal{N}(s)$, and therefore $\sum_{j\in\mathcal{N}(s)} \omega_{sj} V_j \geq V_s$, which contradicts Eq. (24).

Therefore, neither an ordinary node nor the source node can be a strict local minimum. Consequently, no non-sink node of the SSQRN is a strict local minimum. □

3.3 Equipotential regions and existence of a descending route

The absence of strict local minima does not necessarily imply that every non-sink node has a neighboring node with strictly lower potential. Because of geometric symmetry, two or more adjacent nodes may occasionally have equal potentials. Therefore, equipotential regions should also be considered.

For a node k, define its equipotential component as

$$\mathcal{P}(k) = \big\{ j : j \text{ is connected to } k \quad \text{by a path of nodes with potential } V_k \big\}. \tag{25}$$

The following result shows that such an equipotential region does not create an isolated non-target trap.

Theorem 2 *Let $\mathcal{P}$ be a connected equipotential component of the exact resistor network potential field. If the sink node g does not belong to $\mathcal{P}$, then there exists at least one edge (u, v) such that $u \in \mathcal{P}, v \notin \mathcal{P}, V_v < V_u$.*

Proof Assume, by contradiction, that no node in $\mathcal{P}$ has a neighboring node with lower potential.

First suppose that the source node does not belong to $\mathcal{P}$. Since the entire network is connected and $g \notin \mathcal{P}$, the component $\mathcal{P}$ cannot be the entire network. Hence, there exists at least one boundary edge (u, v) with $u \in \mathcal{P}$ and $v \notin \mathcal{P}$.

Because v is not in the same equipotential component, $V_v \neq V_u$. Under the present assumption that no lower-potential neighbor exists, one must have $V_v > V_u$. The node u is an ordinary node and therefore satisfies the discrete harmonic relation (19). Since at least one neighboring potential is strictly larger than V_u, the weighted-average relation can hold only if another neighboring potential is strictly smaller than V_u. This contradicts the assumption.

If the source node belongs to $\mathcal{P}$, then Eq. (20) implies that the weighted average of its neighboring potentials is strictly smaller than V_s. Hence, at least one neighbor of the source must satisfy $V_j < V_s$, which again contradicts the assumption.

Therefore, every equipotential component that does not contain the sink has at least one exit toward a lower-potential node. □

Theorem 2 leads directly to the following navigation property.

Corollary 1 From every node of the connected SSQRN, there exists a path to the sink along which the potential is non-increasing. Whenever the path leaves an equipotential component that does not contain the sink, the potential decreases strictly.

Proof Starting from an arbitrary node, consider its equipotential component. If the component contains the sink, the sink can be reached through equal-potential edges.

Otherwise, Theorem 2 guarantees the existence of an edge leading to a strictly lower-potential node. The same argument can then be repeated from the new node.

Since the resistor network contains only finitely many nodes, the potential cannot decrease through infinitely many distinct node states without eventually reaching an equipotential

component containing the sink. Therefore, a non-increasing potential path from every node to the sink exists. □

Corollary 1 shows that the steady-state electrical response naturally induces a global orientation toward the current sink while allowing possible equipotential transitions caused by network symmetry.

The discrete network described above can be embedded naturally on a spherical surface. Let R denote the sphere radius. For an internal node $A(x, y)$, define $\varphi_x = \frac{2\pi(x-1)}{n}, \vartheta_y = \frac{\pi y}{m+1}$. Its three-dimensional position is then represented by

$$\mathbf{r}(x, y) = R \begin{bmatrix} \sin\vartheta_y \cos\varphi_x \\ \sin\vartheta_y \sin\varphi_x \\ \cos\vartheta_y \end{bmatrix}. \tag{26}$$

Accordingly, the exact nodal potential derived in Eq. (15) defines a discrete scalar field over the spherical surface. When A_s and A_g are identified as the start and goal positions, respectively, navigation can be interpreted as motion from higher-potential regions toward lower-potential regions.

A basic potential-guided local rule can therefore be written as $k_{t+1} \in \arg\min_{j\in\mathcal{N}(k_t)} V_j$. The above rule illustrates the basic physical mechanism underlying potential-guided navigation and provides the foundation for its subsequent application to path planning.

4 Potential-guided path planning on the spherical grid

Section 3 has established that the exact resistor network potential possesses an intrinsic navigation structure[34–37].

Let $\Omega = \{A(x, y) \mid x = 1, \ldots, n,\ y = 1, \ldots, m\}$ denote the internal nodes of the unfolded spherical grid, with the source $s = A(x_s, y_s)$ and sink $g = A(x_g, y_g)$ interpreted as the start and goal, respectively.

For a fixed network and source–sink pair (s, g), the exact potential $V(x, y)$ derived in Eq. (15) is computed once offline and stored as

$$\mathcal{T}_V = \{(x, y, V(x, y)) \mid A(x, y) \in \Omega\}. \tag{27}$$

During planning, the potential is obtained directly from $\mathcal{T}_V$. Since obstacles are treated only as inaccessible search nodes and do not modify the physical potential field, the same table can be reused for different obstacle configurations as long as (s, g) and the network parameters remain unchanged. A new table is required only when the source or sink changes.

4.1 Composite potential–direction scoring mechanism

Potential values provide global source–sink guidance, whereas an additional target-direction term is introduced to improve local directional consistency. In other words, based on global information, a comprehensive scoring mechanism is used to make local decisions in order to achieve effective path planning.

For a current node p, goal g, and feasible candidate $z \in \mathcal{C}$, define $\mathbf{d}_g = \frac{g-p}{\|g-p\|_2}, \mathbf{d}_z = \frac{z-p}{\|z-p\|_2}$, and the directional deviation

$$D(z) = \frac{1 - \mathbf{d}_g^{\mathrm{T}} \mathbf{d}_z}{2} \in [0, 1]. \tag{28}$$

A smaller $D(z)$ indicates better alignment with the goal direction.

To make the potential term comparable across candidate sets, define $V_{\min} = \min_{q \in \mathcal{C}} V(q), V_{\max} = \max_{q \in \mathcal{C}} V(q)$, and

$$\widehat{V}(z) = \begin{cases} \dfrac{V(z) - V_{\min}}{V_{\max} - V_{\min}}, & V_{\max} > V_{\min}, \\ 0, & V_{\max} = V_{\min}. \end{cases} \tag{29}$$

The final candidate score is

$$F(z) = \widehat{V}(z) + \omega D(z), \qquad z \in \mathcal{C}, \tag{30}$$

where $\omega \geq 0$ controls the contribution of the target-direction term. The candidate with the minimum $F(z)$ is selected preferentially during the subsequent search.

The composite-score procedure is summarized in Algorithm 1.

Algorithm 1 Composite potential–direction score

Require: Current node p; goal g; candidate set $\mathcal{C}$; precomputed potential table $\mathcal{T}_V$; weight $\omega \geq 0$

Ensure: Composite scores $\{F(z) \mid z \in \mathcal{C}\}$

$V_{\min} \leftarrow \min_{z \in \mathcal{C}} V(z)$
$V_{\max} \leftarrow \max_{z \in \mathcal{C}} V(z)$
$\mathbf{d}_g \leftarrow (g - p)/\|g - p\|_2$
for each $z \in \mathcal{C}$ **do**
    if $V_{\max} > V_{\min}$ **then**
        $\widehat{V}(z) \leftarrow \dfrac{V(z) - V_{\min}}{V_{\max} - V_{\min}}$
    else
        $\widehat{V}(z) \leftarrow 0$
    end if
    $\mathbf{d}_z \leftarrow (z - p)/\|z - p\|_2$
    $D(z) \leftarrow \dfrac{1 - \mathbf{d}_g^{\mathrm{T}} \mathbf{d}_z}{2}$
    $F(z) \leftarrow \widehat{V}(z) + \omega D(z)$
end for
return $\{F(z) \mid z \in \mathcal{C}\}$

4.2 RNPG planning method

A conventional eight-neighbor search evaluates all neighboring nodes at each planning step. To reduce unnecessary candidate evaluations, the RNPG planner first restricts the local search to three directions associated with the current heading.

Let $h_t \in \{1, 2, \ldots, 8\}$ denote the discrete heading of the motion at node p_t. The eight headings correspond to the eight standard grid directions E, NE, N, NW, W, SW, S, SE.

The directional candidate set contains the forward direction and the two adjacent directions: $\mathrm{DirSet}(p_t, h_t) = \{h_t - 45°, h_t, h_t + 45°\}$. After obstacle and visited nodes are removed, the feasible directional candidate set becomes $\mathcal{C}_{\mathrm{dir}}(p_t, h_t) = \mathrm{DirSet}(p_t, h_t) \setminus (\mathcal{O} \cup \mathcal{M})$.

At the starting node, the initial discrete heading is determined by the relative coordinate differences between the goal and the start, $h_0 = \mathrm{HeadingToGoal}(s, g)$. In the implementation, this operation quantizes the signs of $x_g - x_s$ and $y_g - y_s$ into one of the eight admissible motion directions.

If $\mathcal{C}_{\mathrm{dir}}(p_t, h_t) \neq \emptyset$, the preferred next node is selected directly from the three-direction candidate set.

If the directional set becomes empty, the search restriction is relaxed and the candidate set is expanded to the complete feasible eight-neighbor set, $\mathcal{C}_8(p_t) = \mathcal{N}_8(p_t) \setminus (\mathcal{O} \cup \mathcal{M})$.

If both the directional candidate set and the full eight-neighbor candidate set are empty, the current node is regarded as a dead end. The planner then removes the current node from the active path and returns to the preceding node.

Let the current active path be $\mathcal{P} = [p_0, p_1, \ldots, p_t]$. When p_t is a dead end, the planner performs

$$\mathcal{P} \leftarrow [p_0, p_1, \ldots, p_{t-1}], \qquad p \leftarrow p_{t-1}. \tag{31}$$

The dead-end node remains in the visited set $\mathcal{M}$ and is therefore not selected again. Once the planner returns to the preceding node, another unvisited branch can be explored. If the path has already returned to the start node and no feasible candidate remains, the algorithm terminates with No Path Found.

Backtracking is used only internally during the search procedure. Nodes removed during backtracking are not retained in the final output path. Consequently, the path delivered to the robot contains only the final collision-free sequence from the start to the goal.

Combining the composite scoring, three-direction search, eight-neighbor correction, and backtracking recovery yields the complete RNPG planner summarized in Algorithm 2.

5 Experimental evaluation

This section evaluates the proposed resistor network potential-guided (RNPG) planner from four aspects. First, the planning efficiency and path quality are examined under different grid sizes. Second, the robustness of the planner is investigated by gradually increasing the obstacle density. Finally, extend this method to dynamic contexts.

All algorithms were implemented in MATLAB and evaluated on the same computer equipped with AMD Ryzen 5 5600 CPU.

Algorithm 2 Potential-guided path planning on the unfolded grid

Require: Grid Ω; obstacles $\mathcal{O}$; start s; goal g; potential table $\mathcal{T}_V$; weight $\omega \geq 0$
Ensure: Collision-free path $\mathcal{P}$, or No Path Found

$p \leftarrow s$, $\mathcal{P} \leftarrow [s]$, $\mathcal{M} \leftarrow \{s\}$
$h \leftarrow \text{HeadingToGoal}(s, g)$
while $p \neq g$ **do**
  $\mathcal{C} \leftarrow \text{DirSet}(p, h) \setminus (\mathcal{O} \cup \mathcal{M})$
  if $\mathcal{C} = \emptyset$ **then**
    $\mathcal{C} \leftarrow \mathcal{N}_8(p) \setminus (\mathcal{O} \cup \mathcal{M})$
  end if
  if $\mathcal{C} \neq \emptyset$ **then**
    $\{F(z) \mid z \in \mathcal{C}\} \leftarrow \text{CompositeScore}(p, g, \mathcal{C}, \mathcal{T}_V, \omega)$ ▷ Algorithm 1
    $\mathcal{C}^* \leftarrow \arg\min_{z \in \mathcal{C}} F(z)$
    if $|\mathcal{C}^*| > 1$ **then**
      $\mathcal{C}^* \leftarrow \arg\min_{z \in \mathcal{C}^*} V(z)$
    end if
    $p^+ \leftarrow \arg\min_{z \in \mathcal{C}^*} \|z - g\|_2$
    $h \leftarrow \text{Heading}(p, p^+)$
    $\mathcal{P} \leftarrow \mathcal{P} \oplus [p^+]$, $\mathcal{M} \leftarrow \mathcal{M} \cup \{p^+\}$, $p \leftarrow p^+$
  else
    if $|\mathcal{P}| = 1$ **then**
      return No Path Found
    end if
    Remove the last node from $\mathcal{P}$; $p \leftarrow \text{last}(\mathcal{P})$
    if $|\mathcal{P}| > 1$ **then**
      $h \leftarrow \text{Heading}(\mathcal{P}_{|\mathcal{P}|-1}, \mathcal{P}_{|\mathcal{P}|})$
    else
      $h \leftarrow \text{HeadingToGoal}(s, g)$
    end if
  end if
end while
return $\mathcal{P}$

5.1 Scalability and path-quality comparison

This experiment evaluates the planning performance as the map size increases. Four unfolded-grid sizes, $30\times30, 50\times50, 70\times70, 100\times100$, are considered, while the obstacle density is fixed at 20%. For each grid size, 100 feasible random maps are generated. The proposed RNPG method is compared with A*, JPS, and Dijkstra.

Four metrics are used to evaluate the planning performance: search time T_{search}, unfolded-grid path length L_{grid}, spherical path length $L_{\mathbb{S}}$, and planning success rate SR. The unfolded-grid path length is calculated as

$$L_{\text{grid}} = N_{\text{hv}} + \sqrt{2}\, N_{\text{diag}}, \tag{32}$$

Table 2: Scalability of different planners under 20% obstacle density. R_{grid} and $R_{\mathbb{S}}$ denote the median RNPG-to-A* path-length ratios over the same 100 maps.

	Time (ms)				Path-length ratio	
Grid	RNPG	A*	JPS	Dijkstra	R_{grid}	$R_{\mathbb{S}}$
30×30	0.344	1.338	0.548	12.418	1.076	1.012
50×50	0.578	2.514	1.438	105.757	1.065	1.011
70×70	0.824	4.022	2.485	424.253	1.100	1.022
100×100	1.168	7.908	5.186	2185.358	1.096	1.038

where N_{hv} and N_{diag} denote the numbers of horizontal/vertical and diagonal moves, respectively. After a planned path is mapped back onto the spherical surface, its geometric length is evaluated by

$$L_{\mathbb{S}} = \sum_{i=1}^{K-1} R \arccos\left(\frac{\mathbf{r}_i^{\mathrm{T}} \mathbf{r}_{i+1}}{R^2}\right), \tag{33}$$

where $\mathbf{r}_i$ is the three-dimensional position of the ith path node and $R = 1$ in all experiments. The success rate is defined as $SR = \frac{N_{\text{success}}}{N_{\text{total}}} \times 100\%$. To quantify the path-quality difference between RNPG and the shortest-path baseline, the pairwise ratios

$$\rho_{\text{grid}} = \frac{L_{\text{grid}}^{\text{RNPG}}}{L_{\text{grid}}^{A^*}}, \qquad \rho_{\mathbb{S}} = \frac{L_{\mathbb{S}}^{\text{RNPG}}}{L_{\mathbb{S}}^{A^*}} \tag{34}$$

are computed on the same test maps, and their medians are reported. Under the unified eight-connected motion model, A*, JPS, and Dijkstra return identical optimal unfolded-grid costs up to numerical roundoff.

Therefore, A* is used as the representative shortest-path baseline for the relative path-length analysis, avoiding redundant comparisons among equivalent optimal grid-cost baselines. Table 2 summarizes the scalability results under20% obstacle density.

As can be seen from the table, all four methods achieve a 100% success rate at every tested scale.

The median search time of RNPG increases from 3.44×10^{-4} s at 30×30 to 1.17×10^{-3} s at 100×100, indicating a relatively mild increase with map size. At the largest tested scale, the median runtimes of A*, JPS, and Dijkstra are 7.91 ms, 5.19 ms, and 2.19 s, respectively, whereas RNPG requires only 1.17 ms. Accordingly, under the adopted MATLAB implementations, RNPG is approximately 6.77 times faster than A*, 4.44 times faster than JPS, and 1.87×10^3 times faster than Dijkstra at 100×100. Compared with A*, RNPG increases the grid path length by less than 10%, while the difference in the corresponding spherical path length remains within approximately 4%. Overall, RNPG achieves a favorable balance between planning efficiency and path quality.

Figure 4 intuitively presents the experimental results.

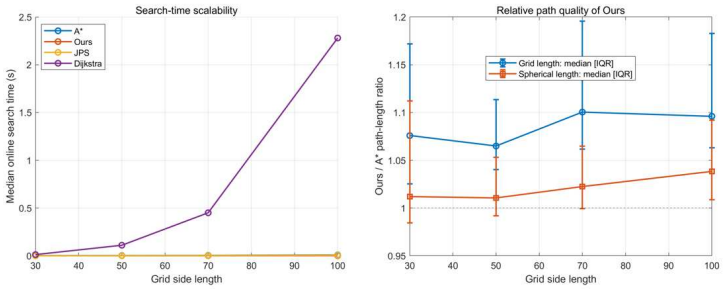


Fig. 4: Statistical comparison under increasing grid size with 20% obstacle density. Each scale contains 100 feasible random maps.

Figure 5 presents a representative path-planning case under the same obstacle configuration.

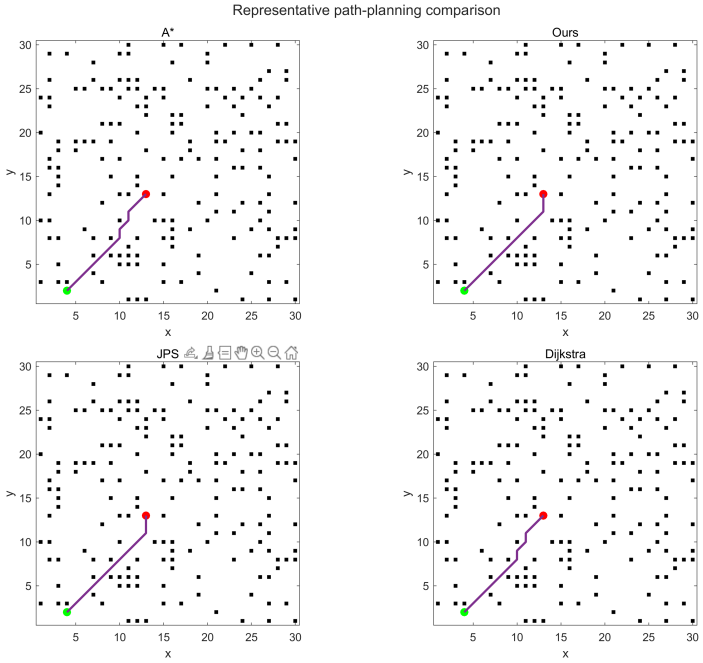


Fig. 5: Representative path-planning results of A*, RNPG, JPS, and Dijkstra on the same 30×30 obstacle map.

All compared methods successfully generate collision-free paths from the start to the goal. Although the resulting trajectories differ slightly because of their distinct search strategies, RNPG follows a route comparable to those of the shortest-path baselines while requiring substantially less search time.

5.2 Robustness to obstacle density

The next experiment investigates the influence of environmental complexity on planner performance. The grid size is fixed at 100×100, while the obstacle density is increased from 5% to 30% in increments of 5%. For each density, 100 feasible random maps are generated using the same source–goal pair and the same precomputed potential table, resulting in 600 test cases in total. The results are shown in Figure 6.

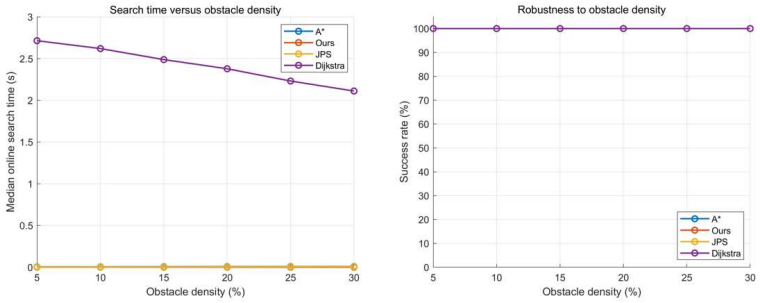


Fig. 6: Planning performance under increasing obstacle density on a 100×100 grid.

All four planners achieve a 100% success rate over all tested maps. The corresponding numerical results are summarized in Figure 7.

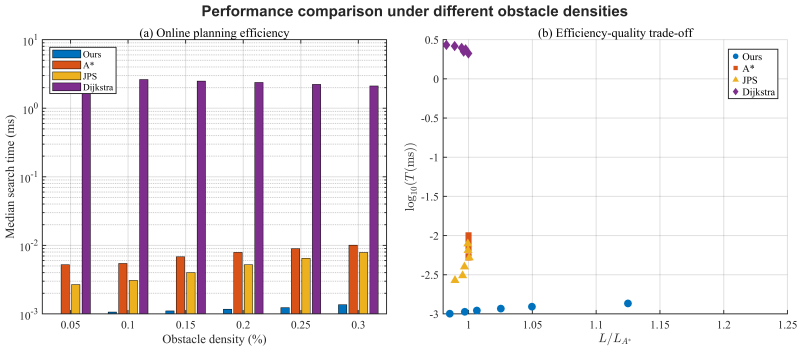


Fig. 7: Performance comparison under different obstacle densities. (a) Median online search time of RNPG and baseline planners. (b) Efficiency–quality trade-off measured by runtime ratio and spherical path-length ratio with respect to A*.

As shown in Figure 7(a), RNPG consistently achieves the lowest online search time under different obstacle densities. Although the computational costs of A* and JPS increase with environmental complexity, RNPG maintains a relatively stable latency due to the utilization of the precomputed physical potential field. Figure 7(b) further demonstrates the efficiency–quality trade-off. RNPG achieves a substantial reduction in computational cost while maintaining a spherical path length close to A*. These results indicate that RNPG effectively balances planning efficiency and path quality.

5.3 Dynamic-obstacle extension and validation

The preceding experiments consider static obstacle configurations. To further examine the adaptability of the proposed RNPG framework, the planner is extended to environments with moving obstacles.

5.3.1 Representative dense dynamic environment

To visualize the behavior of Dynamic RNPG under a relatively crowded environment, a 30×30 unfolded grid is constructed with a total obstacle density of 20%. Moving obstacles account for 20% of all obstacles, corresponding to 36 dynamic obstacles and 144 static obstacles. Equivalently, dynamic obstacles occupy 4% of the complete grid. A representative successful scenario is shown in Figure 8.

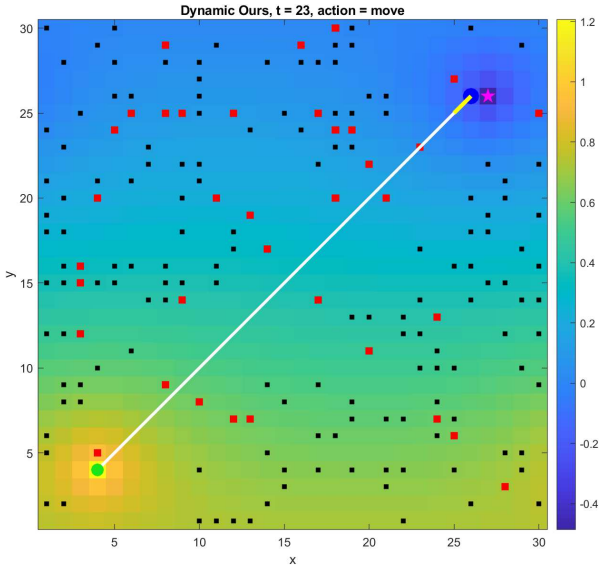


Fig. 8: Representative Dynamic RNPG execution in a dense moving-obstacle environment.

Black squares represent static obstacles, red squares represent moving obstacles, the blue circle indicates the current robot position, and the magenta star denotes the goal. The white curve shows the executed trajectory accumulated up to the current time step.

5.3.2 Validation of the recovery mechanisms

Unlike the static case, RNPG does not permanently exclude previously visited nodes when handling dynamic environments. Instead, it adopts a short-term tabu memory mechanism, allowing the planner to revisit regions that become feasible again. To address temporary blockages and local dead-ends, three recovery mechanisms are

introduced. When the preferred direction is temporarily blocked, the robot first waits for a limited number of steps. If the directional candidate set becomes unavailable, the search is expanded to the complete eight-neighbor set. If no feasible neighboring node exists, the planner backtracks to a previously safe node and continues the search. After detouring or recovery operations, the heading direction is reoriented toward the goal. In this way, the dynamic extension preserves the offline potential guidance while adapting only to local feasibility changes.

To distinguish the roles of the three recovery strategies more clearly, three controlled mechanism-isolation experiments are additionally performed. The corresponding results are illustrated in Figure 9.

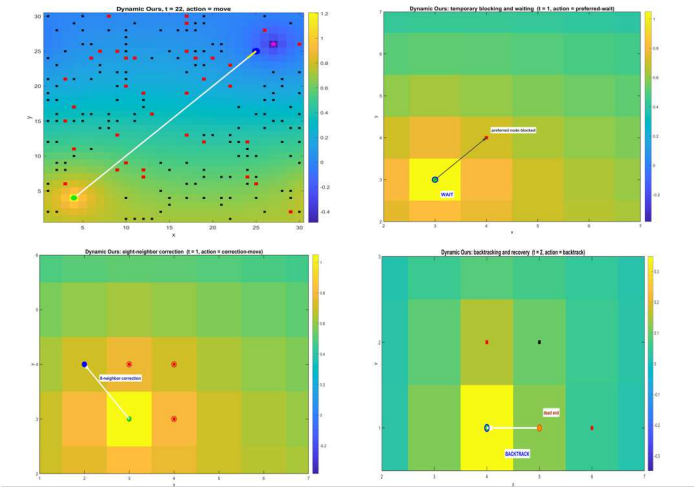


Fig. 9: Illustration of the dynamic recovery mechanisms of the proposed RNPG planner.

Figure 9(a) shows the overall RNPG trajectory in a representative dynamic environment and serves as a reference for the three recovery mechanisms illustrated in Figures 9(b)–(d).

Figure 9(b) illustrates the waiting mechanism. When the RNPG-preferred node is temporarily occupied by a moving obstacle, the robot waits at its current position instead of immediately taking a longer detour. After two waiting steps, the obstacle moves away and the robot continues along the original route. The goal is reached in 27 decision steps, including 25 movements and two waits. Since waiting does not change the robot position, the executed and retained path lengths are identical, with $L_{\text{exec}} = L_{\text{final}} = 33.284$.

Figure 9(c) shows the eight-neighbor correction mechanism. When all three preferred directional candidates are blocked, i.e., $\mathcal{C}_{\text{dir},t} = \varnothing, \mathcal{C}_{8,t} \neq \varnothing$, the planner temporarily expands the search to the full eight-neighbor set. In this scenario, two correction moves are triggered, and the robot reaches the goal in 24 decision steps without waiting or backtracking. The executed and retained path lengths are both

$L_{\text{exec}} = L_{\text{final}} = 25.657$. This mechanism therefore allows RNPG to bypass short-term directional blockages while preserving forward progress.

Figure 9(d) illustrates the backtracking mechanism. The robot first enters a branch that later becomes infeasible. When neither the directional candidate set nor the eight-neighbor set contains a feasible next node, the robot returns to the previous safe node and searches again. After the obstacle configuration changes, a new feasible direction becomes available and the robot proceeds toward the goal. The goal is reached in 14 decision steps, with one backtracking operation and two eight-neighbor corrections.

Because the robot physically enters and then leaves the failed branch, the executed trajectory is longer than the final retained route: $L_{\text{exec}} = 17.728, L_{\text{final}} = 15.728$. Their difference of 2 corresponds to the additional outward and return motions caused by the backtracking operation. This confirms that the backtracking mechanism is actually activated during execution.

Table 3 shows that the three mechanisms perform different and complementary functions.

Table 3: Mechanism-validation results for the dynamic RNPG extension. All three scenarios were successfully completed.

Scenario	Steps	Mechanism count			Path length	
		Wait	Corr.	Back.	L_{exec}	L_{final}
Temporary crossing	27	2	0	0	33.284	33.284
Directional blocking	24	0	2	0	25.657	25.657
Dynamic dead-end	14	0	2	1	17.728	15.728

These results verify that the dynamic extension is not simply the static RNPG algorithm applied repeatedly to a changing map. Instead, it introduces a hierarchical recovery structure while retaining the same precomputed exact potential field. The waiting mechanism handles short-lived conflicts with minimal geometric disturbance, the eight-neighbor correction provides local directional flexibility, and backtracking enables recovery from temporary dead ends.

6 Conclusion and future work

This work establishes a unified framework that integrates exact potential of SSQRN with resistor network potential-guided path planning. Starting from a discrete SSQRN model, the exact expression of the nodal potential under source–sink excitation is derived by exploiting the structure and spectral representation of the network Laplacian. On this basis, the contribution of the special polar boundary is further incorporated through a correction term, yielding a complete exact physical potential field that accounts for the full boundary effect.

Based on this exact potential field, its navigation properties are further investigated. By using the discrete Kirchhoff relation and the weighted mean-value property of nodal potentials, it is shown that no non-sink node can be a strict local minimum of the potential field in a connected positive-resistance network. Furthermore, for any equipotential connected component that does not contain the sink, there exists at

least one boundary edge leading to a node with strictly lower potential. These results reveal the intrinsic descending navigation structure of the resistor network potential field and provide a mathematical basis for using it as a global physical navigation field.

On this foundation, a resistor network potential-guided planning method, denoted as RNPG, is proposed on the unfolded spherical grid. The method transforms the global connectivity information encoded in the exact physical potential field into lightweight local motion decisions. Experimental results show that RNPG achieves higher planning efficiency than the compared methods while maintaining stable planning success rates and reasonable path quality. Furthermore, RNPG is extended to dynamic-obstacle environments, and the roles of waiting, eight-neighbor correction, and backtracking are verified in handling temporary blockages and locally blocked situations. Overall, RNPG combines high planning efficiency with good real-time responsiveness, while its navigation decisions are based on resistor network potential fields, providing strong physical interpretability.

Future work will investigate the mathematical modeling and exact potential solutions of more complex curved surfaces and network structures, and will systematically analyze the intrinsic relationships among network topology, resistance parameters, and potential-navigation properties. The current validation involving dynamic obstacles, multiple start–goal pairs, and robot simulations remains preliminary. Subsequent work will further improve the local recovery and dynamic adaptation mechanisms of RNPG and extend the framework to more complex dynamic environments, multi-robot coordination, and continuous motion constraints.

7 Data availability

The data that support the findings of this study are available from the corresponding author upon reasonable request.

References

[1] Hadad, Y., Soric, J.C., Khanikaev, A.B., *et al.*: Self-induced topological protection in nonlinear circuit arrays. Nat. Electron. **1**(3), 178–182 (2018)

[2] Lüpke, F., Eschbach, M., Heider, T., *et al.*: Electrical resistance of individual defects at a topological insulator surface. Nat. Commun. **8**(1), 15704 (2017)

[3] Novoselov, K.S., Geim, A.K., Morozov, S.V., *et al.*: Electric field effect in atomically thin carbon films. Science **306**(5696), 666–669 (2004)

[4] Novoselov, K.S., Geim, A.K., Morozov, S.V., *et al.*: Two-dimensional gas of massless Dirac fermions in graphene. Nature **438**(7065), 197–200 (2005)

[5] Darwish, M., Boysan, H., Liewald, C., *et al.*: A resistor network simulation model for laser-scanning photo-current microscopy to quantify low conductance regions in organic thin films. Org. Electron. **62**, 474–480 (2018)

[6] Xu, G., Eleftheriades, G.V., Hum, S.V.: Analysis and design of general printed circuit board metagratings with an equivalent circuit model approach. IEEE Trans. Antennas Propag. **69**(8), 4657–4669 (2021)

[7] Hum, S.V., Du, B.Z.: Equivalent circuit modeling for reflectarrays using floquet modal expansion. IEEE Trans. Antennas Propag. **65**(3), 1131–1140 (2017)

[8] Rhazaoui, K., Cai, Q., Adjiman, C.S., *et al.*: Towards the 3d modeling of the effective conductivity of solid oxide fuel cell electrodes: I. model development. Chem. Eng. Sci. **99**, 161–170 (2013)

[9] Zhang, D., Yang, B., Tan, J.P., *et al.*: Impact damage localization and mode identification of cfrps panels using an electric resistance change method. Compos. Struct. **276**, 114587 (2021)

[10] Jeon, S.J., Lee, J.S., Kim, Y.J., *et al.*: Electrical analysis method for gamma-ray imaging system based on resistive network readout. IEEE Trans. Nucl. Sci. **68**(9), 2392–2399 (2021)

[11] Kirchhoff, G.: Ueber die auflösung der gleichungen, auf welche man bei der untersuchung der linearen vertheilung galvanischer ströme geführt wird. Ann. Phys. **148**(12), 497–508 (1847)

[12] Wu, F.Y.: The potts model on a cayley tree. J. Phys. A Math. Gen. **37**, 6653 (2004)

[13] Izmailian, N.S., Kenna, R.: A generalised formulation of the laplacian approach to resistor networks. J. Stat Mech. Theory Exp. **2014**(9), 09016 (2014)

[14] Sundas, R., Baig, N.A., Njuguna, J., Rahman, K., Fough, N.: Underwater target detection analysis using spherical acoustic sensor arrays. In: 2024 IEEE International Workshop on Metrology for the Sea; Learning to Measure Sea Health Parameters (MetroSea), pp. 240–245 (2024). IEEE

[15] Jia, G., Chen, Y., Tu, J., Zhang, D.: A method for predicting sensitivity of spherical hydrophones at high hydrostatic pressures and its experimental validations. The Journal of the Acoustical Society of America **158**(3), 2011–2021 (2025)

[16] Gözükara, A.C., Ceylan, U.A.: Numerical method for predicting transient aerodynamic heating in hemispherical domes. Computation **12**(8), 162 (2024)

[17] Bommes, D., Lévy, B., Pietroni, N., Puppo, E., Silva, C., Tarini, M., Zorin, D.: Quad-mesh generation and processing: A survey. In: Computer Graphics Forum, vol. 32, pp. 51–76 (2013). Wiley Online Library

[18] Campen, M.: Partitioning surfaces into quadrilateral patches: A survey. In: Computer Graphics Forum, vol. 36, pp. 567–588 (2017). Wiley Online Library

[19] Zhao, H.: A scientist question: Research on the impact of super structured quadrilateral meshes on convergence and accuracy of finite element analysis. arXiv preprint arXiv:2507.17184 (2025)

[20] Millán, A.P., Sun, H., Giambagli, L., Muolo, R., Carletti, T., Torres, J.J., Radicchi, F., Kurths, J., Bianconi, G.: Topology shapes dynamics of higher-order networks. Nature Physics, 1–9 (2025)

[21] Bianconi, G.: Higher-order Networks. Cambridge University Press, ??? (2021)

[22] Dijkstra, E.W.: A note on two problems in connexion with graphs. In: Edsger Wybe Dijkstra: His Life, Work, and Legacy, pp. 287–290 (2022)

[23] Hart, P.E., Nilsson, N.J., Raphael, B.: A formal basis for the heuristic determination of minimum cost paths. IEEE transactions on Systems Science and Cybernetics **4**(2), 100–107 (1968)

[24] Harabor, D., Grastien, A.: Online graph pruning for pathfinding on grid maps. In: Proceedings of the AAAI Conference on Artificial Intelligence, vol. 25, pp. 1114–1119 (2011)

[25] Liu, L.X., Wang, X., Yang, X., *et al.*: Path planning techniques for mobile robots: Review and prospect. Expert Syst. Appl. **227**, 120254 (2023)

[26] Patle, B.K., Pandey, A., Parhi, D.R.K., *et al.*: A review: On path planning strategies for navigation of mobile robot. Def. Technol. **15**(4), 582–606 (2019)

[27] Yang, L., Li, P., Qian, S., *et al.*: Path planning technique for mobile robots: A review. Machines **11**(10), 980 (2023)

[28] Aybars, U.: Path planning on a cuboid using genetic algorithms. Inf. Sci. **178**(16), 3275–3287 (2008)

[29] Fu, Z., Zhao, Y.Z., Qian, Z.Y., *et al.*: Wall-climbing robot path planning for testing cylindrical oilcan weld based on voronoi diagram. In: 2006 IEEE/RSJ International Conference on Intelligent Robots and Systems, pp. 2749–2753 (2006). IEEE

[30] Mazaheri, H., Goli, S., Nourollah, A.: Path planning in three-dimensional space based on butterfly optimization algorithm. Sci. Rep. **14**(1), 2332 (2024)

[31] Kulathunga, G.: A reinforcement learning based path planning approach in 3d environment. Procedia Comput. Sci. **212**, 152–160 (2022)

[32] Lian, Y., Xiao, X., Zhang, J., Jin, L., Yu, J., Sun, Z.: Neural dynamics for cooperative motion control of omnidirectional mobile manipulators in the presence of noises: A distributed approach. IEEE/CAA Journal of Automatica Sinica **11**(7), 1605–1620 (2024)

[33] Xie, Z., Liu, M., Su, Z., Sun, Z., Jin, L.: A data-driven obstacle avoidance scheme for redundant robots with unknown structures. IEEE Transactions on Industrial Informatics, 1793–1802 (2024)

[34] Jiang, X., Dai, J., Zheng, Y., Jiang, Z.: Analysis of double Beltrami horn surface resistor networks and efficient path planning. Knowledge-Based Systems **338**, 115489 (2026)

[35] Jiang, X., Dai, J., Zheng, Y., Jiang, Z.: Modeling of omnidirectional antenna space radiation shaped resistor networks and efficient path planning. Applied Physics Reviews **12**(4), 041405 (2025)

[36] Jiang, X., Guan, Y., Zheng, Y., Jiang, Z., Liu, Z.: Robot path planning base on potential function of a resistor network. Applied Mathematical Modelling **151**, 116534 (2025)

[37] Zhang, C., Jiang, X., Zheng, Y., Jiang, Z.: Structured zeroing neural network solution for the mathematical model of a fan dynamic resistor network and its applications. Physica A: Statistical Mechanics and its Applications **689**, 131418 (2026)